Research Article | Vol. 25, No. 21 | 16 Oct 2017 | OPTICS EXPRESS 24861
Optics EXPRESS

On chip chirality-distinguishing beamsplitter

FENGCHUN ZHANG,[1,3,4] YAO LIANG,[2,4] HERAN ZHANG,[1] CHONG LEI,[2] JIAYANG WU,[2] NING ZHU,[3] SHUWEN ZHENG,[3] YONG ZHANG,[3] XU-GUANG HUANG,[1,*] BAOHUA JIA,[2,5] AND SONGHAO LIU[1,3]

[1]*Guangzhou Key Laboratory for Special Fiber Photonic Devices and Applications, South China Normal University, Guangzhou, 510006, China*
[2]*Centre for Micro-Photonics, Faculty of Science, Engineering and Technology, Swinburne University of Technology, Hawthorn, Victoria 3122, Australia*
[3]*Guangdong Provincial Key Laboratory of Nanophotonic Functional Materials and Devices, Guangdong Engineering Technology Research Center of Low Carbon and Advanced Energy Materials, Institute of Opto-Electronic Materials and Technology, South China Normal University, Guangzhou, 510631, China*
[4]*These authors contributed equally to this work*
[5]*bjia@swin.edu.au*
**huangxg@scnu.edu.cn*

Abstract: The chirality of photons plays a fundamental role in light-matter interactions. However, a limiting factor in photonic integrated circuits is the lack of a miniaturized component, which can distinguish the chirality in a low cost and integrated manner. Herein we numerically demonstrate a chirality-distinguishing beamsplitter that can address this challenge. It consists of an integrated polarization rotator and a linear polarization beamsplitter, which together can fulfill the task of distinguishing and splitting left- and right-handed quasi-circularly polarized modes on a chip with an ultra-broadband operation range from 1.45 μm to 1.65 μm. Owning to the reciprocity, the device can emit photons with selectable spin angular momentum depending on the chosen feeding waveguide. The device is compatible with complementary metal-oxide semiconductor technology and it may open up new avenues in the fields of on-chip nano-photonics, bio-photonics and quantum information science.

© 2017 Optical Society of America

OCIS codes: (130.3120) Integrated optics devices; (230.1360) Beam splitters; (230.7370) Waveguides; (350.5030) Phase; (260.1440) Birefringence; (260.5430) Polarization.

References and links

1. R. A. Beth, "Mechanical Detection and Measurement of the Angular Momentum of Light," Phys. Rev. **50**(2), 115–125 (1936).
2. K. Y. Bliokh, D. Smirnova, and F. Nori, "Quantum spin Hall effect of light," Science **348**(6242), 1448–1451 (2015).
3. C. Leyder, M. Romanelli, J. P. Karr, E. Giacobino, T. C. H. Liew, M. M. Glazov, A. V. Kavokin, G. Malpuech, and A. Bramati, "Observation of the optical spin Hall effect," Nat. Phys. **3**(9), 628–631 (2007).
4. X. Yin, Z. Ye, J. Rho, Y. Wang, and X. Zhang, "Photonic spin Hall effect at metasurfaces," Science **339**(6126), 1405–1407 (2013).
5. R. Farshchi, M. Ramsteiner, J. Herfort, A. Tahraoui, and H. T. Grahn, "Optical communication of spin information between light emitting diodes," Appl. Phys. Lett. **98**(16), 162508 (2011).
6. Y. Zhao, J. S. Edgar, G. D. Jeffries, D. McGloin, and D. T. Chiu, "Spin-to-orbital angular momentum conversion in a strongly focused optical beam," Phys. Rev. Lett. **99**(7), 073901 (2007).
7. M. Khorasaninejad, W. T. Chen, A. Y. Zhu, J. Oh, R. C. Devlin, D. Rousso, and F. Capasso, "Multispectral Chiral Imaging with a Metalens," Nano Lett. **16**(7), 4595–4600 (2016).
8. C. D. Stanciu, F. Hansteen, A. V. Kimel, A. Kirilyuk, A. Tsukamoto, A. Itoh, and T. Rasing, "All-optical magnetic recording with circularly polarized light," Phys. Rev. Lett. **99**(4), 047601 (2007).
9. D. F. Phillips, A. Fleischhauer, A. Mair, R. L. Walsworth, and M. D. Lukin, "Storage of light in atomic vapor," Phys. Rev. Lett. **86**(5), 783–786 (2001).
10. K. F. Mak, K. He, J. Shan, and T. F. Heinz, "Control of valley polarization in monolayer MoS2 by optical helicity," Nat. Nanotechnol. **7**(8), 494–498 (2012).
11. M. D. Turner, M. Saba, Q. M. Zhang, B. P. Cumming, G. E. Schroder-Turk, and M. Gu, "Miniature chiral beamsplitter based on gyroid photonic crystals," Nat. Photonics **7**(10), 801–805 (2013).

#301438 https://doi.org/10.1364/OE.25.024861
Journal © 2017 Received 30 Jun 2017; revised 14 Sep 2017; accepted 22 Sep 2017; published 2 Oct 2017

Optics EXPRESS

12. H. Liang, L. Zhang, S. Zhang, T. Cao, A. Alù, S. Ruan, and C.-W. Qiu, "Gate-Programmable Electro-Optical Addressing Array of Graphene-Coated Nanowires with Sub-10 nm Resolution," ACS Photonics **3**(10), 1847–1853 (2016).
13. J. K. Gansel, M. Thiel, M. S. Rill, M. Decker, K. Bade, V. Saile, G. von Freymann, S. Linden, and M. Wegener, "Gold helix photonic metamaterial as broadband circular polarizer," Science **325**(5947), 1513–1515 (2009).
14. J. Lin, J. P. Mueller, Q. Wang, G. Yuan, N. Antoniou, X. C. Yuan, and F. Capasso, "Polarization-controlled tunable directional coupling of surface plasmon polaritons," Science **340**(6130), 331–334 (2013).
15. M. Khorasaninejad and K. B. Crozier, "Silicon nanofin grating as a miniature chirality-distinguishing beam-splitter," Nat. Commun. **5**, 5386 (2014).
16. Y. Ke, Y. Liu, Y. He, J. Zhou, H. Luo, and S. Wen, "Realization of spin-dependent splitting with arbitrary intensity patterns based on all-dielectric metasurfaces," Appl. Phys. Lett. **107**(4), 041107 (2015).
17. D. Lin, P. Fan, E. Hasman, and M. L. Brongersma, "Dielectric gradient metasurface optical elements," Science **345**(6194), 298–302 (2014).
18. M. Schnell, P. Sarriugarte, T. Neuman, A. B. Khanikaev, G. Shvets, J. Aizpurua, and R. Hillenbrand, "Real-Space Mapping of the Chiral Near-Field Distributions in Spiral Antennas and Planar Metasurfaces," Nano Lett. **16**(1), 663–670 (2016).
19. Y. Yang, R. C. da Costa, M. J. Fuchter, and A. J. Campbell, "Circularly polarized light detection by a chiral organic semiconductor transistor," Nat. Photonics **7**(8), 634–638 (2013).
20. W. Li, Z. J. Coppens, L. V. Besteiro, W. Wang, A. O. Govorov, and J. Valentine, "Circularly polarized light detection with hot electrons in chiral plasmonic metamaterials," Nat. Commun. **6**, 8379 (2015).
21. Y. Cui, L. Kang, S. Lan, S. Rodrigues, and W. Cai, "Giant chiral optical response from a twisted-arc metamaterial," Nano Lett. **14**(2), 1021–1025 (2014).
22. M. Esposito, V. Tasco, F. Todisco, M. Cuscunà, A. Benedetti, D. Sanvitto, and A. Passaseo, "Triple-helical nanowires by tomographic rotatory growth for chiral photonics," Nat. Commun. **6**, 6484 (2015).
23. Y. Fang, R. Verre, L. Shao, P. Nordlander, and M. Käll, "Hot Electron Generation and Cathodoluminescence Nanoscopy of Chiral Split Ring Resonators," Nano Lett. **16**(8), 5183–5190 (2016).
24. J. Petersen, J. Volz, and A. Rauschenbeutel, "Chiral nanophotonic waveguide interface based on spin-orbit interaction of light," Science **346**(6205), 67–71 (2014).
25. R. Mitsch, C. Sayrin, B. Albrecht, P. Schneeweiss, and A. Rauschenbeutel, "Quantum state-controlled directional spontaneous emission of photons into a nanophotonic waveguide," Nat. Commun. **5**, 5713 (2014).
26. Y. Lefier and T. Grosjean, "Unidirectional sub-diffraction waveguiding based on optical spin-orbit coupling in subwavelength plasmonic waveguides," Opt. Lett. **40**(12), 2890–2893 (2015).
27. R. J. Coles, D. M. Price, J. E. Dixon, B. Royall, E. Clarke, P. Kok, M. S. Skolnick, A. M. Fox, and M. N. Makhonin, "Chirality of nanophotonic waveguide with embedded quantum emitter for unidirectional spin transfer," Nat. Commun. **7**, 11183 (2016).
28. F. J. Rodríguez-Fortuño, I. Barber-Sanz, D. Puerto, A. Griol, and A. Martínez, "Resolving Light Handedness with an on-Chip Silicon Microdisk," ACS Photonics **1**(9), 762–767 (2014).
29. K. Y. Bliokh, F. J. Rodríguez-Fortuño, F. Nori, and A. V. Zayats, "Spin–orbit interactions of light," Nat. Photonics **9**(12), 796–808 (2015).
30. R. F. Oulton, V. J. Sorger, D. A. Genov, D. F. P. Pile, and X. Zhang, "A hybrid plasmonic waveguide for subwavelength confinement and long-range propagation," Nat. Photonics **2**(8), 496–500 (2008).
31. L. Feng, M. Ayache, J. Huang, Y. L. Xu, M. H. Lu, Y. F. Chen, Y. Fainman, and A. Scherer, "Nonreciprocal light propagation in a silicon photonic circuit," Science **333**(6043), 729–733 (2011).
32. Y. Liang and X. Huang, "Generation of two beams of light carrying spin and orbital angular momenta of opposite handedness," Opt. Lett. **39**(17), 5074–5077 (2014).
33. Y. Luo, M. Chamanzar, A. Apuzzo, R. Salas-Montiel, K. N. Nguyen, S. Blaize, and A. Adibi, "On-chip hybrid photonic-plasmonic light concentrator for nanofocusing in an integrated silicon photonics platform," Nano Lett. **15**(2), 849–856 (2015).
34. Y. Liang, H. W. Wu, B. J. Huang, and X. G. Huang, "Light beams with selective angular momentum generated by hybrid plasmonic waveguides," Nanoscale **6**(21), 12360–12365 (2014).
35. F. Zhang, Y. Liang, H. Zhang, Y. Zhang, X.-G. Huang, B. Jia, and S. Liu, "Optical gears in a nanophotonic directional coupler," Opt. Express **25**(10), 10972–10983 (2017).
36. A. Yariv, "Coupled-mode theory for guided-wave optics," IEEE J. Quantum Electron. **9**(9), 919–933 (1973).
37. Y. Liang, F. Zhang, J. Gu, X. G. Huang, and S. Liu, "Integratable quarter-wave plates enable one-way angular momentum conversion," Sci. Rep. **6**(1), 24959 (2016).
38. H. R. Zhang, F. C. Zhang, Y. Liang, X. G. Huang, and B. H. Jia, "Diodelike asymmetric transmission in hybrid plasmonic waveguides via breaking polarization symmetry," J. Phys. D Appl. Phys. **50**(16), 165104 (2017).
39. D. Dai and H. Wu, "Realization of a compact polarization splitter-rotator on silicon," Opt. Lett. **41**(10), 2346–2349 (2016).
40. Z. Liu, Y. Qiu, Q. Yang, and J. Tao, "Ultracompact wavelength and polarization directional coupler based on nanowire waveguides," J. Mod. Opt. **64**(15), 1538–1543 (2017).

Optics EXPRESS

1. Introduction

It was demonstrated more than 80 years ago that the circularly polarized light (CPL) is associated with spin angular momentum (SAM), with each photon carrying ± ħ, depending on the chirality of circular polarization [1]. Recently, the spin of photons has been gathering widely interest in the field of chiral nanophotonics, where the handedness of photons has significant influences on the outcomes, for example, photonic spin Hall effect (PSHE) [2–4], spin optical communication [5], spin orbital interactions [6], chiral imaging [7], all-optical magnetic recording [8], optical storage [9], and dynamic valley polarization controlling [10] to name just a few. Although to distinguish the chirality of photons holds the key to the applications and effects mentioned above, it is particularly challenging due to the low circular birefringence for naturally available materials [11]. Meanwhile, with the trend towards designing compact footprint photonic integrated circuits (PICs), the CPL mode with an ultra-high resolution have great potentials in some realistic applications [12], so the need to distinguish and separate left- or right-handed circularly polarized (LCP or RCP) light on a chip becomes increasingly desired in both science and engineering.

In recent years, several methods and platforms were used for distinguishing the chirality of photons, such as metamaterials [11, 13], metasurfaces [7, 14–18], photonic spin Hall effect [2–4], chiral photon detector [19,20], circular dichroism (CD) spectrum [21–23], and photonic integrated circuits (PICs) based on nanophotonic waveguide structures [24–28]. However, all demonstrations above have been restricted to light in free space, which is a major limitation for many potential applications in integrated optics. To date, despite investigations of various extraordinary SAM in the evanescent field of nanophotonic waveguide structures [24, 29], little attention has been paid to separate photons of different chirality in a nanophotonic waveguide system. Thus, it remains an ongoing challenge.

Hybrid plasmonic waveguides [30] are fundamentally important building blocks for PICs due to their extraordinary characteristics, such as considerable birefringence effect, subwavelength confinement with low loss transmission and polarization control, which have been validly investigated in many integrated optical systems [30–34]. Thus, by steering birefringence effect and polarization rotation effect of hybrid plasmonic waveguides it provides a great potential for on chip PICs to distinguish photons with opposite SAM.

In this work, we present an integrated chirality-distinguishing beamsplitter (CDBS) that can address the challenge of distinguishing RCP and LCP photons. The underlying physical mechanism is based on the combination of polarization rotation and polarization splitting. In contrast with the sophisticated 3D chiral metamaterial, our proposed device only consists of a hybrid plasmonic polarization rotator (HP-PR) and a linear polarization beamsplitter (PBS). This integrateable CDBS, to our knowledge, is the first time to be reported. The device, if further integrated with two waveguide detectors at the output ports, will be able to make a fully-integrated chiral photon detector and may open up new avenues for optical manipulation, sensing and quantum information computing on a chip. The rest of this paper are organized as follows. In section 2, the overall concept for designing the device is presented. In sections 3 and 4, the HP-PR and linear PBS structures are detailedly demonstrated respectively. Then, the performances of the CDBS are illustrated in section 5. Finally, the conclusions are given in section 6.

2. The overall concept and the simulation settings

For a circularly polarized light with an arbitrary handedness, a left-handed polarized beam or a right-handed polarized one, it is very difficult to distinguish its handedness via a simple linear waveguide because the electric vector of the beam is always spinning continuously. However, the circularly polarized light can be treated as a combination of two orthogonal linear polarized components (parallel and perpendicular to the fast axis) with the same amplitude and a $\pm \pi/2$ phase difference depending on the handedness. When a CPL beam travels through a quarter-wave plate (QWP), there will be another $\pi/2$ phase difference accumulation. Thus,

Optics EXPRESS

when the two opposite handedness quasi-CPL beams travel through the QWP structure successively, at the output port of the QWP, the phase difference between the two orthogonal linear components will become to be respectively π and 0 depending on its handedness, which leads to the two synthesized beams at the output port are linearly polarized and mutually orthogonal. Then, via a linear polarization beamsplitter, the two orthogonal synthesized linear beams can be split into different channels. That gives a chance to distinguish the handedness of CPL.

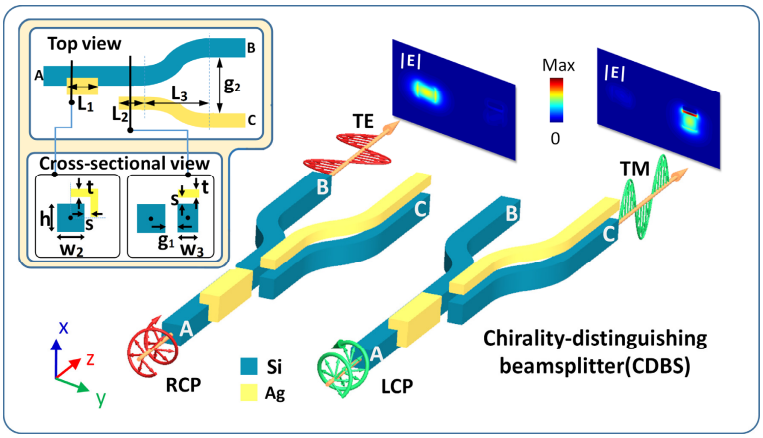

Fig. 1. 3D schematics (not to scale) of the proposed CDBS and the coordinate system used. A quasi-RCP mode (the electric vector spinning clockwise from the point view of the source) launched at the input port-A is transformed into a horizontal mode (quasi-TE) and output from the left output port-B. Correspondingly, a quasi-LCP mode launched at port-A is converted into a vertical mode (quasi-TM) and output from the other output port-C. The inserted figure describes the top view, cross-sectional view and the parameter details, and the black circles denote the centers of these corresponding structures. The proposed device is surrounded by silica (SiO_2), which is not shown for simplicity.

Based on the above consideration, we proposed a new integrated CDBS device of which basic structure and schematic diagram are shown in Fig. 1. The device is composed of two sections, a HP-PR (actually a QWP) and a linear PBS. The whole structures are surrounded by silica (*SiO2*), which is not shown for simplicity.

In addition, we utilized the finite-different time-domain method (FDTD solutions, a commercial software from lumerical Inc) to validate and optimize these ideas. The simulation domain was divided into congruent cubes one another in all directions, and the mesh spacing in the transverse (*x* and *y* directions) and longitudinal (*z* direction) are all *0.01 μm*. In addition, the effective mode indices of different structure sections are calculated using mode solver simulations (FDTD Solutions mode source). Also, the mesh spacing employed for transverse is *0.01 μm*. The boundary conditions in all the simulations process are chosen to be perfectly matching layer (PML). The working wavelength is set to be λ = 1.55 μm, and the refractive indices of silver (*Ag*), silicon (*Si*), and silica employed in this work are $[n_{\_Ag}, n_{\_Si}, n_{\_SiO2}] = [0.5397 + 10.8229i, 3.4764 + 0i, 1.4440 + 0i]$.

3. The integrated polarization rotator

In this section, we choose a hybrid plasmonic structure as a polarization rotator to realize the polarization rotation function. Comparing with the all-dielectric structure, the hybrid plasmonic one can effectively downsize the footprint of device due to its high birefringence [34]. For the HP-PR, it contains a nanophotonic core with the same width (w_2) and height (h) for transmitting the quasi-CPL modes, and on the right top of it, there is an L-shaped *Ag* structure with length (L_1) and thickness (t). As an important parameter of the hybrid plasmonic waveguide, a SiO_2 spacer [thickness (s)] is needed between *Si* core and L-shaped *Ag* structure (Fig. 1).

Optics EXPRESS

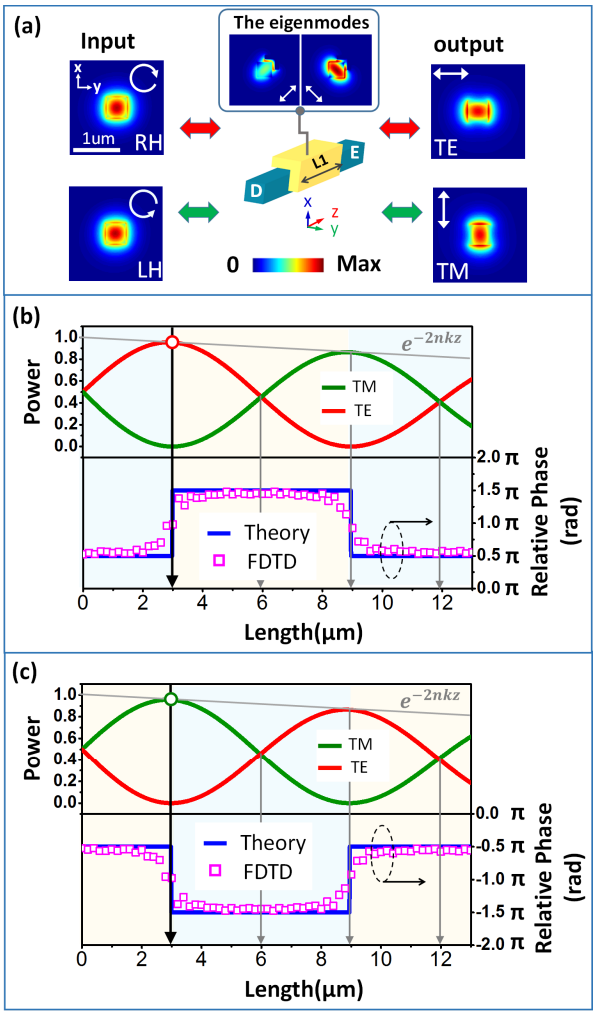

Fig. 2. (a) The schematic of the modes conversion: from port D to E, quasi-CPL modes are converted into quasi linearly polarized light (quasi-LPL) modes correspondingly (a σ_R mode to a quasi-TE mode and a σ_L mode to a quasi-TM mode). On the contrary, from E to D, quasi linearly polarized light (quasi-LPL) modes are converted into quasi-CPL modes due to the reciprocity. The insert picture shows the eigenmodes of the hybrid structure. These white arrow lines represent the polarization states of beams. **(b)** and **(c)** The theoretical and FDTD simulated results (power and relative phase) of the σ_R or σ_L mode transmitting in the hybrid plasmonic HP-PR (QWP) structure, respectively.

In a nanophotonic system, a quasi-CPL mode can be excited by coupling a circularly polarized light into a square cross-sectional nanophotonic waveguide. Similar to the CPL in free space, a quasi-CPL mode can be decomposed into two equal-amplitude orthogonally polarized components (quasi-TE and -TM modes) with a relative phase of $\Delta\phi_0 = \pm\,^{\pi}/2$ between them depending on the handedness. In our case, the quasi-TE and -TM modes are defined as $\boldsymbol{E_{TE}} = exp(-i\omega t + ink_0x)\boldsymbol{e_{TE}}$ and $\boldsymbol{E_{TM}} = exp(-i\omega t + ink_0x + \Delta\phi_0)\boldsymbol{e_{TM}}$ respectively ($\boldsymbol{e_{TE/TM}}$ are the unit vectors of the quasi-TE and -TM modes). We use the descriptions of $\boldsymbol{\sigma_L} = |\Delta\phi_0, \pi/2\rangle$ for a quasi-LCP mode and $\boldsymbol{\sigma_R} = |\Delta\phi_0, -\pi/2\rangle$ for a quasi-RCP one. The word "quasi-" means that in this non-paraxial case, the fundamental *0th* order eigenmodes (quasi-TE and -TM modes) in the nanophotonic waveguides are not purely transverse and inevitably have some longitudinal electric field component (E_z) [35].

Optics EXPRESS

In fact, due to the symmetry of the hybrid QWP structure, the eigenmodes in HP-PR are shown in the middle of Fig. 2(a), their polarization angles are $\varphi = \pm \pi/4$, where φ is the angle down from the positive x-axis. For λ = 1.55μm, the effective indices of corresponding eigenmodes can be solved respectively as $n_{\pi/4} = 2.4375 + 0.002265i$ and $n_{-\pi/4} = 2.3075 + 0.001497i$, by utilizing the eigenmode solver in FDTD solutions.

When the quasi-CPL modes propagate in the hybrid plasmonic QWP, the $\boldsymbol{\sigma}_R$ and $\boldsymbol{\sigma}_L$ modes undergo different polarization conversion processes. The $\boldsymbol{\sigma}_R$ mode will be converted into a quasi-TE mode while the $\boldsymbol{\sigma}_L$ mode will be transformed into a quasi-TM one. These results are illustrated in Fig. 2(a).

By solving the coupled mode equations [36, 37], the power evolution of quasi-TE/-TM modes in the hybrid plasmonic HP-PR, P_{TE} and P_{TM}, can be described as

$$\begin{cases} P_{TE} = \left| -i \sin\left(\kappa z + \dfrac{\Delta\phi_0}{2} \right) \right|^2 \bullet \exp(-2\bar{n}k_0 z) \\ P_{TM} = \left| \cos\left(\kappa z + \dfrac{\Delta\phi_0}{2} \right) \right|^2 \bullet \exp(-2\bar{n}k_0 z) \end{cases}, \tag{1}$$

where $\kappa = \pi/(2L_c)$ is the propagation constant, L_c the coupling length, $\Delta\phi_0$ the initial relative phase between quasi-TM mode and quasi-TE mode as mentioned before [in our case, for a $\boldsymbol{\sigma}_L$ mode input, $\Delta\phi_0 = \pi/2$; for a $\boldsymbol{\sigma}_R$ one, $\Delta\phi_0 = -\pi/2$], The term $\exp(-2\bar{n}k_0 z)$ denotes the propagation loss, $\bar{n} = [Im(n_{\pi/4}) + Im(n_{-\pi/4})]/2$, $k_0 = 2\pi/\lambda$ the wave number in free space. The $-i$ item indicates that there is an intrinsic $-\pi/2$ phase lag between the two orthogonal modes (quasi-TE and quasi-TM modes).

To illustrate the polarization rotation effect clearly, we need to calculate the coupling length (L_c), which is a crucial physical parameter described by

$$L_c = \frac{\pi}{[\mathrm{Re}(n_{\pi/4}) - \mathrm{Re}(n_{-\pi/4})]k_0}, \tag{2}$$

$\mathrm{Re}(n_{\pi/4})$ and $\mathrm{Re}(n_{-\pi/4})$ are the real part of the effective refractive index of the corresponding eigenmodes. From Eq. (2), one can get the coupling length of $L_c = 5.96\ \mu m$, which is the length of a half-wave plate [38]. In our case, the HP-PR actually is a QWP structure, so the length of hybrid waveguides should be precisely $L_2 = L_c/2 = 2.98\ \mu m$, which is a good agreement with the FDTD simulation result of 2.90 μm. The dependence of energy (power) of quasi-TE and -TM modes on the length of the HP-PR structure for $\boldsymbol{\sigma}_R$ and $\boldsymbol{\sigma}_L$ modes are shown, respectively in Figs. 2(b) and 2(c). When the length of HP-PR is set to be 2.90 μm, at the output port-E, the $\boldsymbol{\sigma}_R$ mode is converted into a quasi-TE mode completely [Fig. 2(b)] and the $\boldsymbol{\sigma}_L$ mode is transformed into a quasi-TM mode entirely [Fig. 2(c)]. These results give us a chance to split the two orthogonal modes using a linear beamsplitter, which will be discussed in the following section.

For the phase evolution process, we describe the relative phase of quasi-TM and -TE components of the incident $\boldsymbol{\sigma}_L$ and $\boldsymbol{\sigma}_R$ modes, respectively, in Figs. 2(b) and 2(c). The relative phase between two orthogonal linearly polarized modes is defined as

$$\Delta\phi(z) = \phi_{TM}(z) - \phi_{TE}(z), \tag{3}$$

where $\phi_{TM}(z)$ and $\phi_{TE}(z)$ denote the phases of quasi-TM mode and quasi-TE mode, respectively.

In particular, there is an abrupt π phase jump as the energy of one mode is fully coupled to the other. This is because there are two times of π/2 accumulations when the energy of any dominant linear component is coupled totally from one mode to the other [35]. Meanwhile, one should note that since the e-exponential function is a periodic function with a period of 2π, there is essentially no difference between the relative phase jumps of π or -π in Figs. 2(b) and 2(c). At

Optics EXPRESS

the points where a quasi-TE mode totally converts into a quasi-TM mode, or vice versa, the π-phase shift occurs. Although there are a few differences of the relative phase between the theoretical and the simulated values near the π phase shift points, the power of the quasi-TE (or quasi-TM) mode is much stronger than the other (~0), so that the relative phase mismatch will not significant impact on the results.

4. The linear polarization beamsplitter

The hybrid plasamonic waveguides usually exhibit significant birefringence effect [30], so that one can use the structure to design a linearly PBS for splitting two orthogonal linear polarized light (LPL) beams.

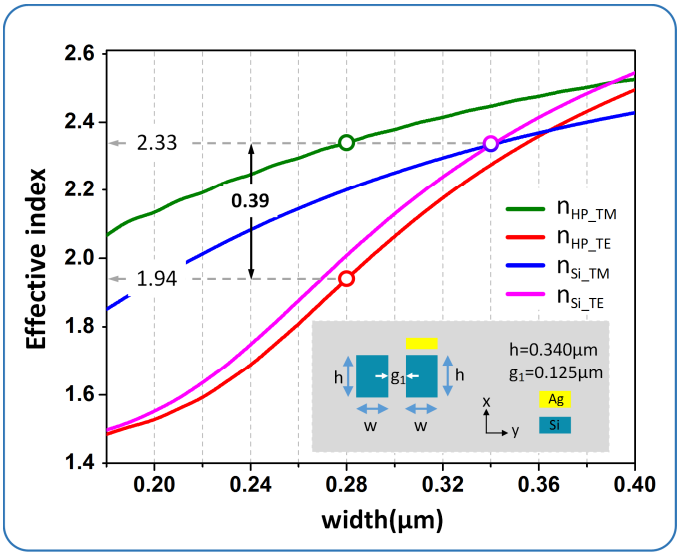

Fig. 3. The dependence of effective index on the width of two waveguides of the PBS structure. The height (h) of each waveguide is *0.34 μm*. n_{HP_TM} and n_{HP_TE} denote the real parts of effective indices for the quasi-TE and -TM mode of the hybrid plasmonic waveguide (HP-WG). Similarly, n_{Si_TM} and n_{Si_TE} are the real parts of the effective indices of the silicon waveguide (Si-WG) corresponding modes.

Figure 3 shows the dependence of effective indices on the width of the waveguides for quasi-TE and -TM modes, assuming the heights of the two waveguides are equal, $h = 0.34\ \mu m$. When the widths (w_2 and w_3) of two waveguides are respectively set to be *0.34 μm* and *0.28 μm*, the effective indices of quasi-TM mode of two waveguides are equal to be *2.33*. However, the effective indices of the quasi-TE modes of two waveguides are significantly different, being *2.33* for silicon waveguide (Si-WG) and *1.94* for hybrid plasmonic waveguide (HP-WG), respectively. Thus, the energy of the quasi-TM mode can be fully coupled between the two WGs of the coupler with a 100% efficiency due to the resonant coupling. Nevertheless, the large difference of effective refractive indices ($\Delta n = 0.39$) for two TE guided modes ensure the quasi-TE mode transmitting mainly in the left *Si* waveguide, due to the non-resonant coupling.

For a two-waveguide coupler structure with large birefringence effect in both horizontal and vertical directions. The coupling lengths of these modes are different. Utilizing supermode theory, the coupling length of the quasi-TE or -TM mode can be written as

$$L_{c\_TE/TM} = \frac{\pi}{[\mathrm{Re}(n_{TE/TM\_even}) - \mathrm{Re}(n_{TE/TM\_odd})]k_0}. \quad (4)$$

Figure 4(a) shows the theoretical prediction of the coupling lengths (L_{C_TM} and L_{C_TE}) and coupling length ratio (L_{C_TM}/L_{C_TE}) of two orthogonal quasi-TE and -TM modes versus the

Optics EXPRESS

different gaps of the coupler. When the gap between two coupled waveguides is set to be g_1 = *0.125 μm*, using the mode solver of the FDTD solutions, the real part of the even and odd modes' effective indices of quasi-TM and quasi-TE modes can be obtained as [Re(n_{TM/TE_even}), Re(n_{TM/TE_odd})] = [*2.4366, 2.3673, 2.2331, 1.9614*]. By solving Eq. (4), one can get the L_{C_TM} (*3.81 μm*) is precisely as twice as the L_{C_TE} (*1.91 μm*), so the value of coupling length ratio is 0.5 [Fig. 4(a)]. Correspondingly, Fig. 4(b) shows the structure configuration of the coupler and the simulation results of the coupling process. From the field distributions of quasi-TE and -TM modes, the coupling region length (L_2) of quasi-TM mode is *(4.27-0.50) μm = 3.77 μm*,which is in a good agreement of the theoretical value of 3.81μm. Thus, when the length of the coupling region is selected to be 3.77 μm, the energy of quasi-TE mode can totally couples back to the left Si-WG, while the energy of the quasi-TM mode is just fully coupled to the right HP-WG due to the phase matching condition [39, 40]. At the end of the coupler, two S-band structures (L_3 = *6μm*, $g_2 = g_1 + 1\mu m = 1.125\mu m$) are used to separate the energies of two orthogonal quasi-LPL modes into different channels (Fig. 1).

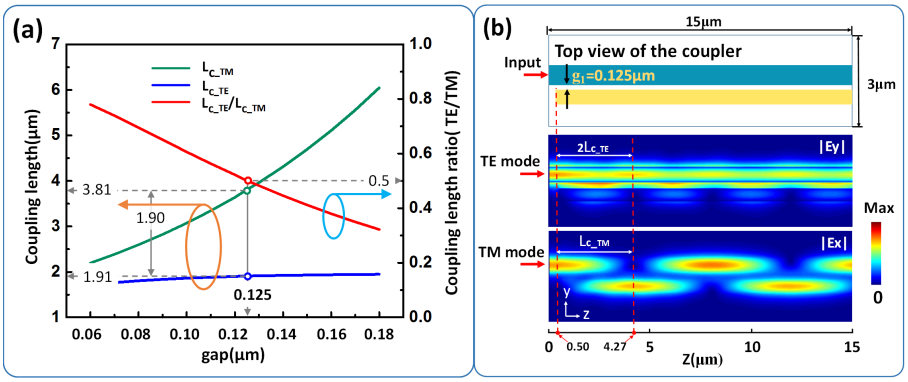

Fig. 4. (a) The theoretical coupling lengths of the quaisi-TE and -TM modes and the coupling length ratio between them. The coupling length ratio equals to 0.5 which means the coupling length of quasi-TM mode is as twice as the one of quasi-TE mode ($L_{c\_TM} = 2L_{c\_TE} = 3.81\mu m$). **(b)** The structure configuration of the coupler and the simulated field distributions ($|E_x|$ and $|E_y|$) of quaisi-TM and -TE modes. The red dotted lines represent that the coupling length of quasi-TM mode is two times as the one of quasi-TE mode ($L_{c\_TM} = 2L_{c\_TE} = 3.77\mu m$), which is in good agreement with the theoretical value.

Because we utilize the S-band structure to decouple two linear orthogonal modes, the structure will inevitably bring some unwanted coupling. Thus, we need to optimize the coupling region length to achieve the best performance. The length of optimized coupling region is represented by L_2, which is shown in Fig. 1. In order to evaluate the performance of the CDBS, firstly, we need to define the Chirality Ratio (CR) of the CDBS by

$$\mathrm{CR} = 10lg(T_{L\_TE} / T_{R\_TM}), \tag{5}$$

where T_{L_TE} and T_{R_TM} are the transmittances of the left and right output ports, individually. It should be noted that, if the value of CR is positive, the input light is a RCP mode. Conversely, if the CR is a negative one, the input light is a LCP mode.

Optics EXPRESS

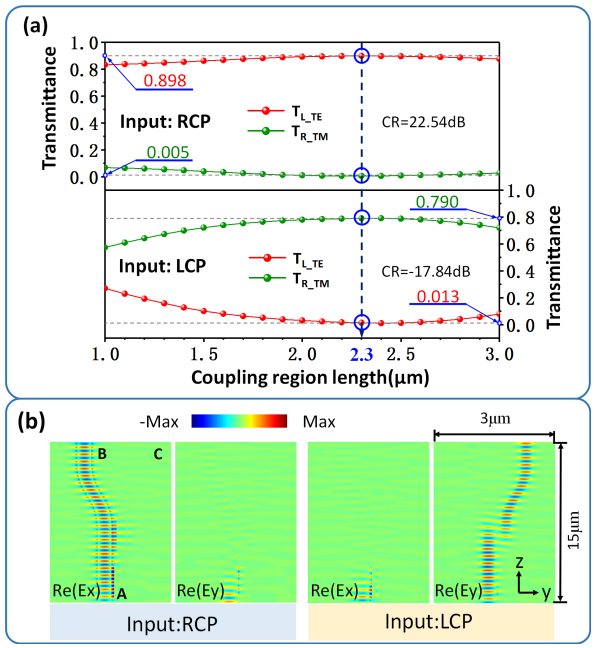

Fig. 5. (a) The transmittances of $\boldsymbol{\sigma}_R$ and $\boldsymbol{\sigma}_L$ modes vary with the coupling region length (L_2). L_2 = *2.3μm* is the optimum length of coupling region (Fig. 1). T_{L_TE} and T_{R_TM} are the normalized transmittance on the left or right branch of the CDBS. **(b)** The corresponding field distributions [Re(E_x) and Re(E_y)] for $\boldsymbol{\sigma}_R$ and $\boldsymbol{\sigma}_L$ modes input respectively. The $\boldsymbol{\sigma}_R$ is converted into a quasi-TE mode (E_x) which propagates in the left Si-WG and outputs from port-B. In contrast, the $\boldsymbol{\sigma}_L$ is transformed into a quasi-TM mode (E_y) which is coupled into the right HP-WG and outputs from port-C.

Figure 5(a) shows our simulation results. When the coupling region length (L_2) is chosen to be *2.3 μm*, the optimum performance is available. From Eq. (5), one can get the CR for $\boldsymbol{\sigma}_R$ input is *22.54 dB* and the one for $\boldsymbol{\sigma}_L$ input is *-17.84 dB*. The corresponding real parts of electric field distributions (E_x and E_y) are shown in Fig. 5(b). For a $\boldsymbol{\sigma}_L$ mode input, the light beam is converted into a quasi-TE (E_x) mode and output from the port-B. In contrast, for a $\boldsymbol{\sigma}_R$ mode input, the light beam is transformed into a quasi-TM (E_y) mode and coupled from the Si-WG into the HP-WG and output from the output port-C. Thus, by comparing the energies of the left and right branches of the CDBS, one can easily know the handedness of the incident quasi-CPL mode. Moreover, the device can split the energies of two orthogonal quasi-CPL modes, which may bring some useful potential for quantum information science and biosensing.

From the above design and discussion, the recommended dimensions of the HP-PR are as follows: The width (w_2) and height (h) of the silicon core are equal: $w_2 = h = 0.34\ \mu m$. The length (L_1) and the thickness (t) of the L-shaped *Ag* structure on the right top of the *Si* core are $L_1 = 2.9\ \mu m$ and $t = 0.1\ \mu m$, respectively. Meanwhile, the thickness of the SiO_2 spacer (s) between *Si* core and L-shaped *Ag* structure is s = 0.06 μm. For the hybrid plasmonic PBS (a directional coupler), the width (w_2) and height (h) of the left Si-WG are equal: $w_2 = h = 0.34\ \mu m$. The right HP-WG has a large birefringence effect on the horizontal (x) and vertical (y) directions, and the width (w_3) and height (h) of the silicon core are *0.28* and *0.34 μm*, respectively. Similarly, the parameters of L-shaped *Ag* strip on top of silicon core are the same as the corresponding ones of HP-PR ($t = 0.1\ \mu m$, $s = 0.06\ \mu m$). The gap (g_1) between two coupled waveguides is $g_1 = 0.125\ \mu m$ and the length of the coupling region is $L_2 = 2.3\ \mu m$. At the end of the coupler, two S-band waveguides are used to decouple two orthogonal linear modes (quasi-TE and -TM) into different channels, whose length and width (gap) are $L_3 = 6\ \mu m$ and $g_2 = 1.125\ \mu m$, respectively. The footprint of the device is less than $13\ \mu m * 2.4\ \mu m$ and these proposed structures are surrounded by SiO_2, which is not shown for simplicity [Fig. 1].

Optics EXPRESS

5. The performances of the CDBS

To test the operation bandwidth of the proposed device, which is one of the fundamental and important properties in practical applications, we performed a wavelength scan from *1.45 μm* to *1.65 μm*. The numerical results are shown in Fig. 6. These results suggest that the device has a broadband characteristic which can distinguish the chirality of photons in the wavelength range from *1.45 μm* to *1.65 μm* for |CR|>*3 dB*.

Owing to the reciprocity, within the same bandwidth, the CDBS can also be used for an SAM-photon emitter, which has the ability to emit photons with selectable SAM. Specifically, in Fig. 1, at port-A, the emitter can emit LCP photons (from the point view of the source) by feeding the Si-WG port-B with a TE mode, and emit RCP photons by launching a TM mode on the HP-WG port-C. One should be noted that this SAM-photon emitter is only an additional functionality of the CDBS and these functionalities of the device may bring some potential for optical communication and molecular detection where the spin-dependent is required.

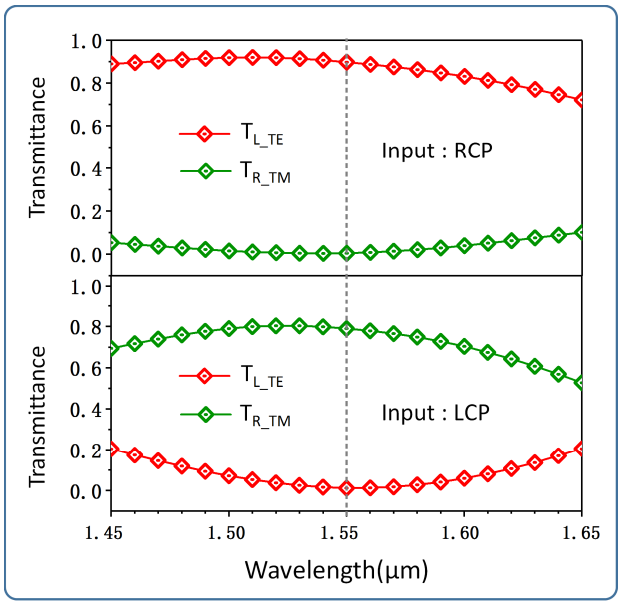

Fig. 6. The transmittance spectrums of $\boldsymbol{\sigma}_R$ and $\boldsymbol{\sigma}_L$ input modes, which denotes that the proposed CDBS has a broadband operation capability from 1.45μm to 1.65μm for |CR|>3dB.

6. Conclusion

In this work, we proposed and numerically demonstrated a novel simple and low-cost nanophotonic device named chirality-distinguishing beamsplitter (CDBS), which has the ability to distinguish and split photons with different chirality on a single photonic chip. Unlike the previous concepts of distinction photons in free-space, our CDBS can distinguish and separate photons with opposite SAM in an integrated chip. Moreover, with the reciprocity, the device can emit opposite handedness of SAM photons, which provides some potential for some applications in which spin-dependent light-matter interactions are involved. Besides, the concept of this work may have influence on spin-optics and may open up a door for some aspects of spin optical communication, chiral molecular detection, on-chip optical interconnection and quantum information processing where photons with opposite SAM are key components and have to be distinguish or generated on an integrated photonic chip.

Optics EXPRESS

Funding

Nature Science Foundation of China (NSFC) (61574064); Natural Science Foundation of Guangdong Province(2014A030313446); the Program for Changjiang Scholars and Innovative Research Team in University (IRT13064); the Science and Technology Planning Project of Guangdong Province (2015B010132009); the Science and Technology Program of Guangzhou (201707010134).

Acknowledgments

Heran Zhang thanks the support of the Innovation Project of Graduate School of South China Normal University.

138.186.72.145 {ts '2017-10-02 21:45:10'}